Chapter

The Asymmetric Flexure Hinge Structures and the Hybrid Excitation Methods for Piezoelectric Stick-Slip Actuators

Tinghai Cheng, Xiaosong Zhang, Xiaohui Lu, Hengyu Li, Qi Gao and Guangda Qiao

Abstract

Piezoelectric stick–slip actuators have become viable candidates for precise positioning and precise metering due to simple structure and long stroke. To improve the performances of the piezoelectric stick–slip actuators, our team deeply studies the actuators from both structural designs and driving methods. In terms of structural designs, the trapezoid-type, asymmetrical flexure hinges and mode conversion piezoelectric stick–slip actuators are proposed to improve the velocity and load based on the asymmetric structure; besides, a piezoelectric stick–slip actuator with a coupled asymmetrical flexure hinge mechanism is also developed to achieve the bidirectional motion. In terms of driving methods, a non-resonant mode smooth driving method (SDM) based on ultrasonic friction reduction is first proposed to restrain the backward motion during the rapid contraction stage. Then, a resonant mode SDM is further developed to improve the output performance of the piezoelectric stick–slip actuator. On this basis, the low voltage and symmetry of the SDM are also discussed. Finally, the direction-guidance hybrid method (DGHM) excitation method is presented to achieve superior performance, especially for high speed.

Keywords: piezoelectric stick–slip actuator, structural design, driving method, flexure hinge mechanism, ultrasonic friction reduction

1. Introduction

Piezoelectric stick–slip actuators have obtained considerable significance and have become the focus area of research for camera focusing mechanisms, cell phones, scanning probe micro-scopes, zoom lens systems and blue-ray devices, because of compact structure, low cost, theoretically unlimited displacement and convenient control [1–3]. Based on the configuration designs, the piezoelectric stick–slip actuators are divided into parallel type [4–6] and non-parallel type [7–9], as illustrated in **Figure 1**.

The parallel type stick–slip actuator means the motion direction of the stator is parallel to that of the slider. For example, Lee et al. presented a stick–slip actuator

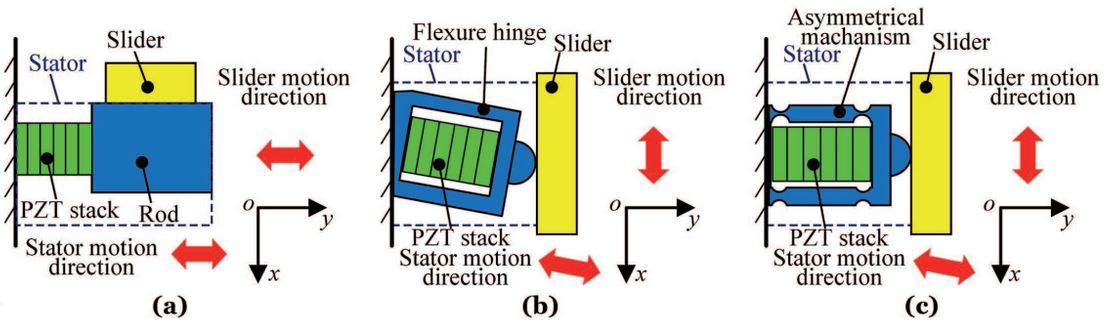

Figure 1.
Schematic diagram of parallel and non-parallel structures. (a) Parallel structure. (b) Non-parallel structure with an angle. (c) Non-parallel structure with asymmetrical flexure hinge.

with the parallel structure using a piezoelectric element and two sliders; and the friction force could be controlled by the spring and the screw [4]. Hunstig et al. proposed a stick–slip actuator with parallel structure, and the friction force was controlled by means of magnets, which could also be predicted by the established friction model [6]. However, the friction force of the parallel type stick–slip actuators cannot be adjusted during the operation, which results in an obvious backward motion. In addition, the velocity and load of such actuators are also seriously restrained.

The piezoelectric stick–slip actuator with non-parallel structure means that there is a movement angle between the stator and the slider. For instance, Li et al. proposed a linear stick–slip actuator with a non-parallel structure based on the lateral motion, which could be generated by a parallelogram-type flexure hinge mechanism and a piezoelectric element [7]. Wen et al. presented a rotary stick–slip actuator with non-parallel structure, and the friction force could be regulated by changing the positive pressure between the slider and stator [9]. Although the velocity and load of the non-parallel type stick–slip actuators are improved relative to the parallel type stick–slip actuators, it is still difficult to meet the actual application requirements. Meanwhile, the backward motions are also generated during the operation. Besides, such actuators are generally structurally asymmetric and perform poor consistency in bidirectional performance.

In this regard, our team focused deeply on the fields of the piezoelectric stick–slip actuators in both structural designs and driving methods. In terms of structural designs, the axial stiffness of the stator is unevenly distributed, and the parasitic motion is generated by introducing the flexure hinge mechanism into the design of the stator, including trapezoid-type piezoelectric stick–slip actuator [10], piezoelectric stick–slip actuators with asymmetrical flexure hinges [11, 12] and mode conversion piezoelectric stick–slip actuator [13]; these structural designs can comprehensively adjust the friction force during the movement of the stick–slip actuator, thereby significantly improving the velocity and load; besides, a coupled asymmetrical flexure hinge mechanism is also developed to achieve the bidirectional motion of the non-parallel type stick–slip actuators [14]. In terms of driving methods, a non-resonant mode smooth driving method (SDM) based on ultrasonic friction reduction is first proposed for the parallel type stick–slip actuator, and the backward motion is restrained during the rapid contraction stage [15]. According to ultrasonic friction reduction, the smaller kinetic friction between the frictional part and the slider can be realized at the resonant frequency. A resonant mode SDM is further developed to improve the performance of the stick–slip actuator [16]. On this basis, the low voltage characteristics and symmetry of the SDM are researched [17, 18]. Finally, a direction-guidance hybrid method (DGHM) is proposed for the non-parallel type stick–slip

actuator with flexure hinge mechanism [19], and the superior performance of this excitation method is achieved, especially for high speed.

2. Development of the asymmetric stator with flexure hinge structures

2.1 Trapezoid-type piezoelectric stick-slip actuator

In this work, a trapezoid-type piezoelectric stick–slip actuator adopts a flexure four-bar mechanism and driving foot with trapezoid beam to obtain the oblique motion, which can make the slider move by oblique displacement of flexure hinge mechanism [10], as shown in **Figure 2**.

The structure diagram of the trapezoid-type piezoelectric stick–slip actuator is illustrated in **Figure 2(a)**. The *ox*, *oy*, and *oz* represent the horizontal, axial and vertical directions, respectively. The actuator is mainly comprised of a flexure hinge mechanism, a slider, a piezoelectric stack, a shim block, a preload screw, a base and a preload mechanism. The preload between the flexure hinge mechanism and

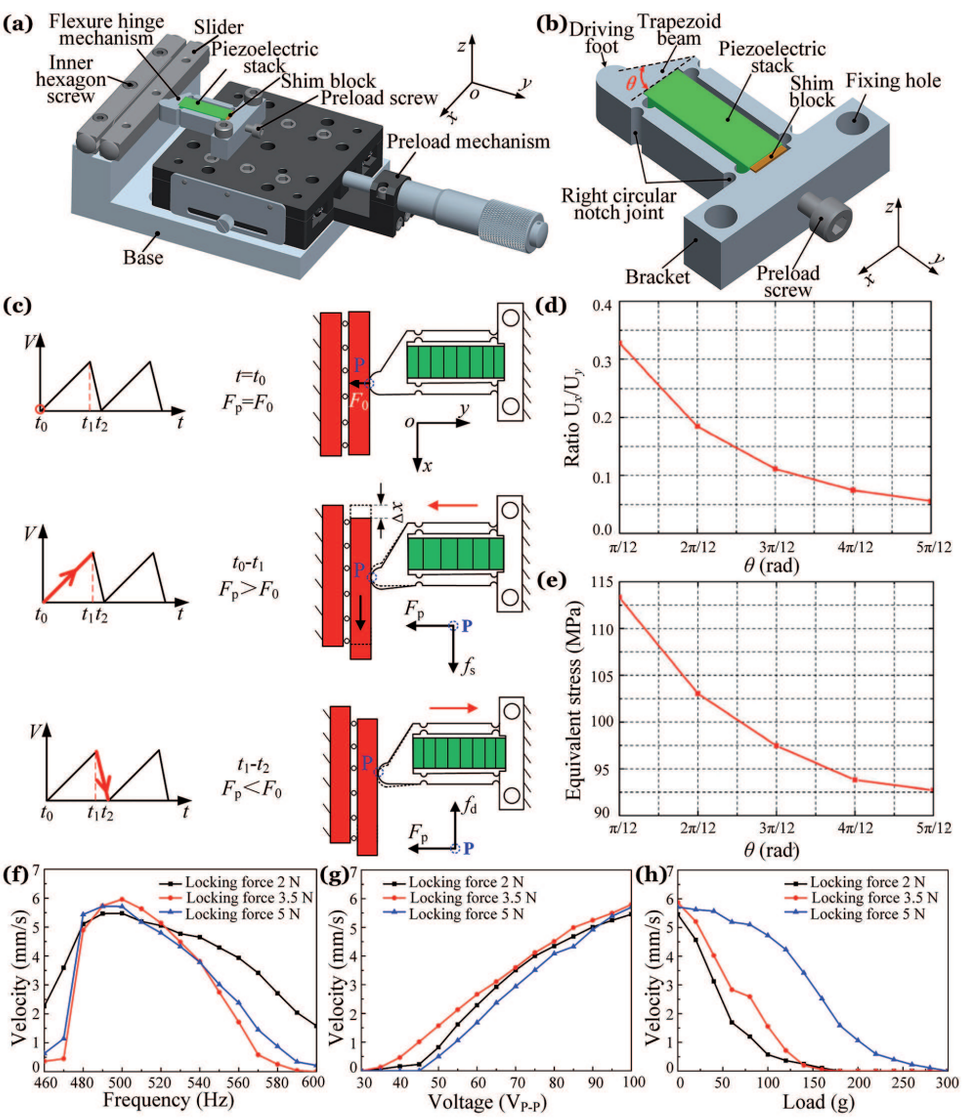

Figure 2.
Research on the trapezoid-type piezoelectric stick–slip actuator. (a) Configuration of the proposed actuator, and (b) the detailed structure of the flexure hinge mechanism. (c) Operation principle of the actuator. (d) and (e) simulation results of the flexure hinge mechanism. (f)–(h) The test results of the actuator. [10].

piezoelectric stack in the initial state is adjusted by the preload screw. The flexure hinge mechanism is preload by the preload mechanism. The needed driving force is generated by the stack which is mounted in the flexure hinge mechanism.

The flexure hinge mechanism is a key component, and its detailed structure is shown in **Figure 2(b)**. The material of the flexure hinge mechanism is AL7075. Four right circular notch joints are employed to the flexure hinge mechanism and thereby the displacement along the axial direction is generated when the piezoelectric stack occurs deformation. It is important that the flexure hinge mechanism utilizes the uneven stiffness distribution of the trapezoid beam to cause needed lateral motion on the driving foot.

The principle of the trapezoid-type stick–slip actuator is depicted in **Figure 2(c)**. In the initial state, when time $t = t_0$, the stack and flexure hinge mechanism keep the original state. The point P is a contact point between the slider and driving foot. The preload force F_0 is equal to F_p generated by the preload mechanism.

1. Slow extension stage ($t_0 \sim t_1$): the stack extends slowly to push the flexure hinge mechanism to expand. In terms of the slider, due to the static friction force f_s between the slider and driving foot, a distance of positive direction is produced on the horizontal axis.

2. Quick contraction stage ($t_1 \sim t_2$): due to the quick contraction of the stack, the flexure hinge mechanism restores to its original condition. And the inertial force makes the condition of the slider remain unchanged.

After the two stages, a small distance of positive direction Δx is generated on the horizontal axis in terms of the slider. The repetition of the above stages makes the actuator generate a long-stroke linear motion.

The lateral displacement of the driving foot can be adjusted by adjusting the angle between the hypotenuse of the trapezoid beam and horizontal axis. To determine the lateral movement on the driving foot, the finite element method (FEM) is used to analyze the angle adjustment process, as shown in **Figure 2(d)** and **(e)**. From the ratio U_x/U_y, a smaller θ rad is needed for better actuation. From the equivalent stress, a larger θ has smaller equivalent stress. Besides, a smaller θ is also essential to meet the requirement of compact size. Finally, $\theta = \pi/6$ rad is selected in this work.

To research the characteristics of the trapezoid-type piezoelectric stick–slip actuator, the prototype and experimental system are established. And a series of experiments are carried out to research the influence of locking force, driving frequency and driving voltage on the performance, as shown in **Figure 2(f)**–**(h)**.

It is worth noting that the locking force between the driving foot and the slider could change the system stiffness and thereby, the optimal frequency appears the slight change. When the voltage is 100 $V_{p\text{-}p}$, and the frequency is inferior to 500 Hz respectively, the velocity rises with the increase of frequency. When the frequency exceeds 500 Hz, the velocity decreases, which results from that the time of deforming to theoretical length is too short for the stack. It can be seen from **Figure 2(f)** that the maximum velocity is 5.96 mm/s under the locking force of 3.5 N. The velocity increases linearly with an increasing voltage. When the voltage is 100 $V_{p\text{-}p}$, and the locking force is 3.5 N respectively, a maximum velocity of 5.96 mm/s is achieved. Meanwhile, when the voltage is 45.17 $V_{p\text{-}p}$, the minimum starting voltage of the actuator, the displacement resolution of 50 nm is achieved under the locking force of 5 N.

In the initial state, the mass of the slider is 35 g. The standard weight is used to measure the load along the horizontal axis of the actuator. The various loads along the positive direction on the horizontal axis are applied in the slider through a pulley and a steel wire. It is conspicuous that the velocity decreases with the

increase in load. The maximum loads of the actuator that can be sustained are 3 N, 1.6 N and 1.6 N when locking forces are 5 N, 3.5 N and 2 N, respectively. The linear relationship between the load and velocity does not emerged, which results from the influence of the assembly errors and the preloading gap.

2.2 Piezoelectric stick-slip actuators using asymmetrical flexure hinges

The trapezoid-type stick–slip actuator developed above can make the slider move by oblique displacement of the flexure hinge mechanism, but it is hard to realize a larger tangential displacement along the motion direction. Therefore, we proposed an idea of using a new four-bar mechanism with different thicknesses of both side flexure hinges, as shown in **Figure 3**. There are considerable improvements in output performance of the actuator based on this design idea.

A four-bar mechanism using asymmetrical flexure hinges is combined with a symmetrical indenter to generate controllable tangential displacement [11]. As shown in **Figure 3(a)**, the stator is mainly comprised of an asymmetrical flexure

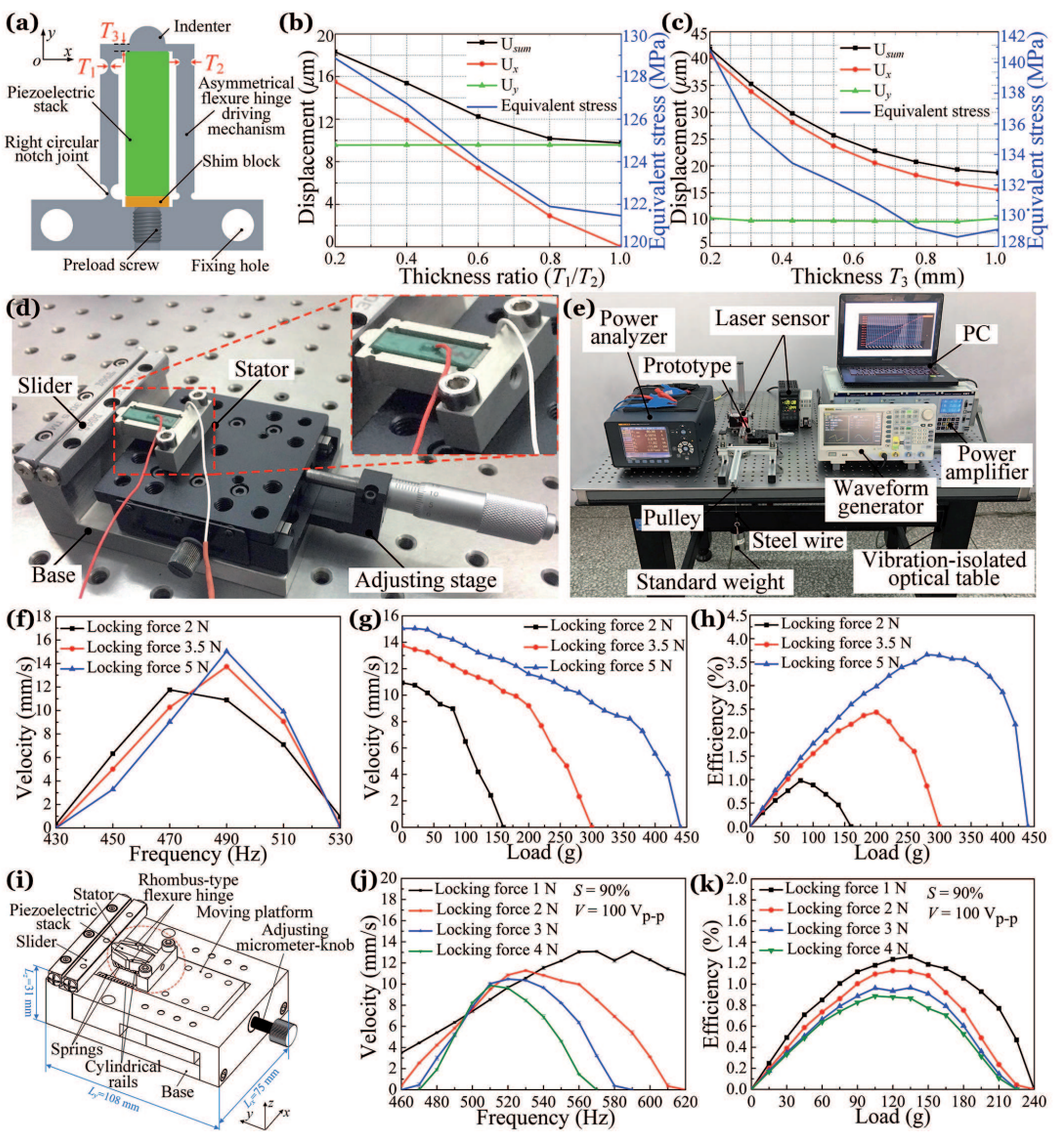

Figure 3.
Research on the piezoelectric stick–slip actuators using asymmetrical flexure hinges. (a) the basic structure of the stator. (b) and (c) simulation results of the asymmetrical flexure hinge mechanism. (d) Prototype and (e) experimental system of the proposed actuator. (f)–(h) The test results of the actuator [11]. (i) The basic structure of the rhombus-type flexure hinge mechanism. (j) and (k) the experimental results of the actuator [12].

hinge driving mechanism, a preload screw, a tungsten chrome steel sheet and a piezoelectric stack. There are right-circle flexure hinges located in both side of the asymmetrical flexure hinge driving mechanism respectively. The thickness of two right-circle flexure hinges on the one side is T_1, and the other side is T_2 ($T_1 \neq T_2$). And the thickness between the stack and the indenter is T_3. By changing the thickness T_1, T_2 and T_3 of the actuators, the oblique movement required by the indenter can be realized.

Deformation of the actuator caused by the different minimum thicknesses of the flexure hinges results in a larger tangential displacement. In the simulation analysis stage, the initial thickness T_1, T_2 and T_3 of the asymmetrical flexure hinge driving mechanism are set as 0.3 mm, 0.3 mm and 4.5 mm, respectively. The simulation results of the asymmetrical flexure hinge driving mechanism under the different ratio of T_1/T_2 and the different thickness of T_3 is shown in **Figure 3(b)** and **(c)**. Based on the results, the mechanism can not only generate the tangential displacement but also change the normal force. Finally, the structure parameters are identified as ratio T_1/T_2 = 0.2 and thickness T_3 = 1 mm.

The actuator mainly consists of a base, a slider, a stator and an adjusting stage, as shown in **Figure 3(d)**. The adjusting stage is used to adjust the preload force between the stator and the slider. The experimental system of the prototype is shown in **Figure 3(e)**. All the experimental equipment is placed on the vibration isolation optical platform.

The experimental results are shown in **Figure 3(f)**–**(h)**. First, when the voltage is 100 $V_{p\text{-}p}$, the velocity is parabolic with the increase of frequency. When the frequency is 470 Hz, and the locking force is 2 N respectively, the obtained maximum velocity of the actuator is 11.75 mm/s. When the locking forces are 3.5 N and 5 N, the obtained maximum velocities of the actuator under the frequency of 490 Hz are 13.72 and 15.04 mm/s, respectively. Besides, the minimum starting voltage is 20.25 $V_{p\text{-}p}$ at the locking force of 3.5 N, and the displacement resolution is 65 nm. Since frictional force drives the slider to produce linear motion, the improvement of the load capacity may be attributed to the increase of frictional forces as the locking force increased. The maximum loads are 160 g, 300 g and 440 g under locking forces of 2 N, 3.5 N and 5 N, respectively. And the maximum efficiency of the actuator under the locking force of 2 N is 0.98% at the load of 80 g. The maximum efficiency of the actuator under the locking force of 3.5 N is 2.43% at the load of 200 g. The maximum efficiency of the actuator under the locking force of 5 N is 3.66% at the load of 280 g.

Furthermore, a rhombus-type flexure hinge mechanism with an asymmetrical structure is proposed [12], which is easy to produce the parasitic motion of the large stroke. The proposed rhombus-type flexure hinge mechanism can improve the velocity of the actuator with a compact stator. The experimental results show that the prototype achieves a maximum velocity of 13.08 mm/s at a frequency of 570 Hz under the voltage of 100 $V_{p\text{-}p}$; and the maximum efficiency is 1.26% with a load of 135 g.

2.3 Mode conversion piezoelectric stick-slip actuator

A novel stick–slip piezoelectric stick–slip actuator based on mode conversion flexure hinge is proposed which is mainly uses the three chutes of the mode conversion flexure hinge to make the driving foot produce lateral displacement [13], as illustrated in **Figure 4(a)** and **(b)**. Under the influence of the symmetrical waveform, the mode conversion flexure hinge can obtain a lateral displacement and push the slider to move a distance.

The mode conversion flexure hinge is comprised of a bracket, a driving foot, four circular notch joins, a beam and three chutes. The deformation of the

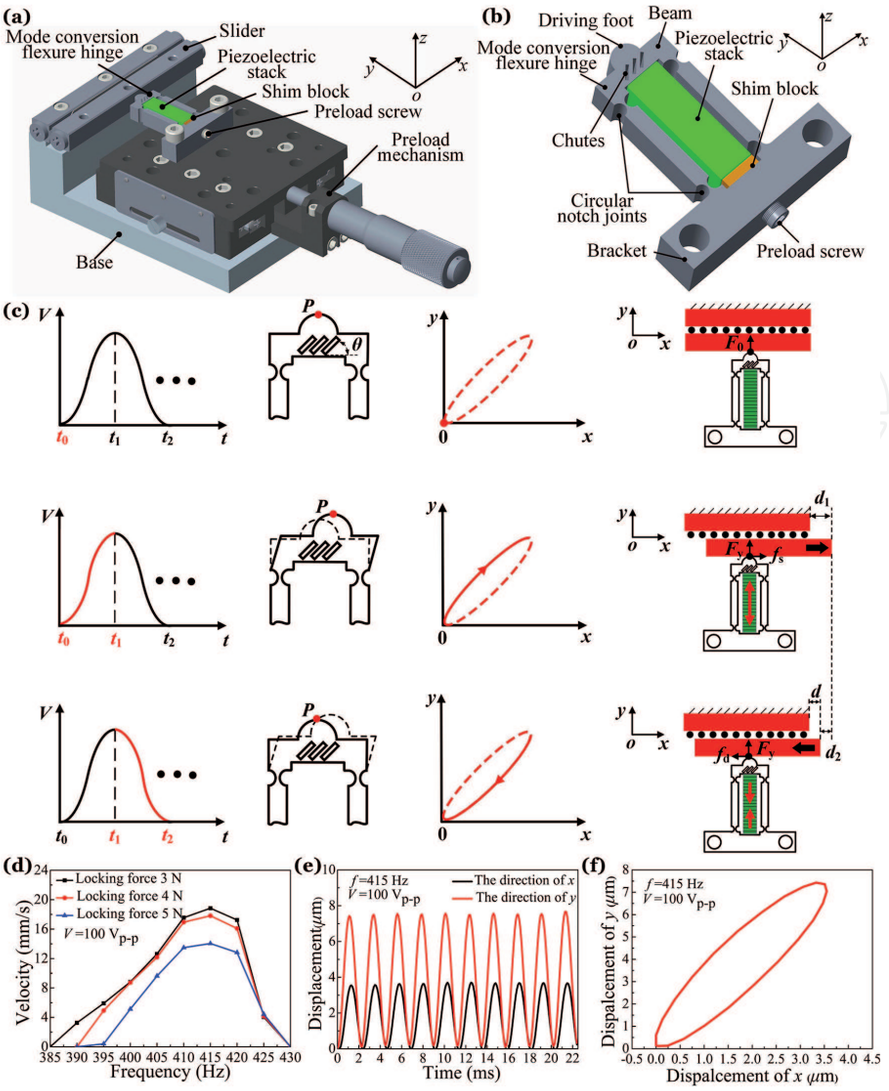

Figure 4.
Research on the mode conversion piezoelectric stick–slip actuator. (a) The detailed structure of the actuator and (b) the stator. (c) Operation principle of the actuator. (d)–(f) The experimental results of the actuator [13].

mode conversion flexure hinge can be produced easily due to four circular notch joins. A symmetrical waveform voltage is chosen to excite the stack. As shown in **Figure 4(c)**, the operation principle of the prototype can be described in the following three steps:

Step 1: no voltage is applied to the stack, and its original length remains. The contact point P is between the driving foot and slider where there is an initial preload force F_0.

Step 2: the point P will generate a displacement of positive directions on both ox and oy axis with the gradual increase of voltage. The pressure force F_y between the mode conversion flexure hinge and slider improves due to the displacement of the positive direction on the oy axis. The slider produces a displacement of the positive direction on the ox axis. Within a certain range, as the pressure force F_y increases, the output force of the actuator will be improved. Thereby, the static friction force f_s makes the slider generate a displacement d_1.

Step 3: the stack restores to its original condition with the decrease of voltage. At this moment, kinetic friction force f_d as a resistance force produces between the mode conversion flexure hinge and the slider. The decrease in pressure force F_y makes the force f_d decrease. Then, a slight back displacement d_2 of the slider is produced, which is opposite to the direction of d_1.

Finally, a displacement of the slider d ($d = d_1$-d_2) is produced. By repeating these steps, the prototype can achieve a large motion in the positive direction of the ox axis.

It is an important parameter for the angle θ of chutes to influent its output performance. Different angles of chutes (30°, 45° and 60°) are applied to the proposed mode conversion flexure hinge, which is simulated by the finite element method to obtain an optimal angle parameter. And the displacement U_x of the point P in the positive direction of the ox axis and the maximum equivalent stress with different angles are listed in **Table 1**. The largest deformation of 2.85 μm is obtained for the ox axis displacement U_x of the point P under the angle of 45°, and the maximum equivalent stress is 105.86 MPa.

With the increase of frequency, the velocity of the prototype first increases and then decreases, whose peak can be reached at 415 Hz, as illustrated in **Figure 4(d)**. For the designed actuator, the maximum velocity of 18.84 mm/s, 17.82 mm/s and 14.04 mm/s are obtained respectively under the locking force of 3 N, 4 N and 5 N.

Moreover, the vibrations and the fitting results in xoy plane of the driving foot are shown in **Figure 4(e)** and **(f)**. An ellipse motion track obtained by the driving foot of the actuator is beneficial to the motion of the slider. It can be seen from experiment results that the maximum velocity and efficiency is 18.84 mm/s and 2.07% when the voltage of the symmetrical waveform and the frequency are 100 $V_{p\text{-}p}$ and of 415 Hz, respectively. Besides, the maximum load and the displacement resolution can reach 360 g and 50 nm in terms of the actuator.

2.4 Bidirectional piezoelectric stick-slip actuator

The asymmetric flexure hinges are generally structurally asymmetric, making it difficult to achieve good consistency in bidirectional output performance. In this work, a coupled asymmetrical flexure hinge mechanism is developed to realize the bidirectional motion of the piezoelectric stick–slip actuator [14], as shown in **Figure 5**.

The bidirectional stick–slip actuator uses coupled asymmetrical flexure hinge mechanisms and symmetrical indenter to generate the controllable tangential displacement. As shown in **Figure 5(a)**, the static simulation of the FEM is used to analyze the deformation of flexure hinges with different sizes. Since a larger oblique displacement will provide better output performance, $A_1 = 1$ mm and $K = A_2/A_3 = 0.2$ with the larger oblique displacement are selected for the final Structure design.

In this section, an MDR-based model is proposed to display the contact and frictional force between the slider and indenter for stick–slip actuators.

The framework of the MDR consists of two preliminary steps to be performed. As shown in **Figure 5(c)**, a one-dimensional profile $g(x)$ and the elastic half-space by an elastic foundation which are in possession of normal stiffness k_y and tangential stiffness k_x is adopted to replace the three-dimensional profile $y = f(x, z)$.

Angle of the chutes	Deformation (μm)	Equivalent stress (MPa)
30°	2.77	106.63
45°	2.85	105.86
60°	2.42	103.32

Table 1.
The simulation results of the proposed actuator.

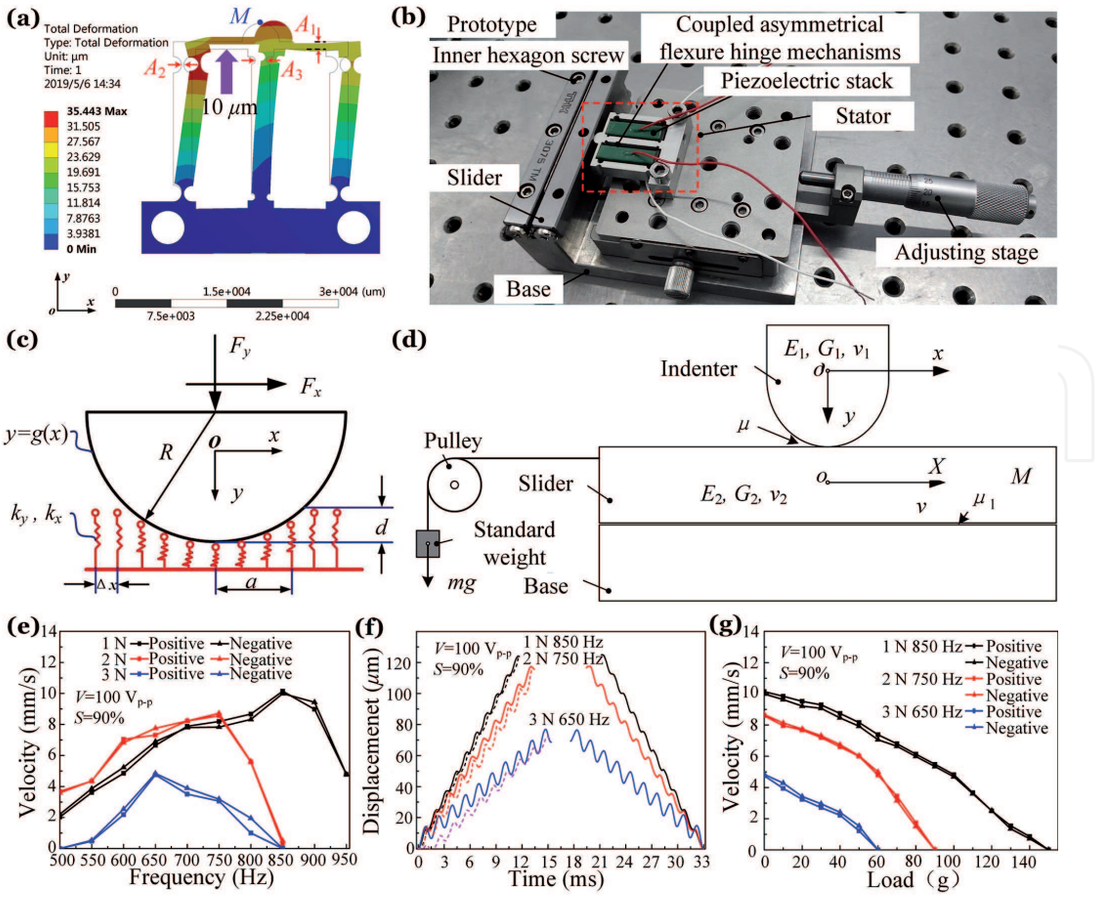

Figure 5.
Research on the bidirectional piezoelectric stick–slip actuator. (a) The static simulation deformation of the flexure hinges. (b) The prototype of the actuator. (c)–(d) MDR model. (e)–(g) The experimental results of the actuator [14].

The stiffness of every individual spring can be expressed as follows:

$$k_y = E^* \Delta x, k_x = G^* \Delta x \tag{1}$$

Δx represents the distance between the springs of elastic foundation, and the effective elastic modulus is defined as:

$$\frac{1}{E^*} = \frac{1-\nu_1^2}{E_1} + \frac{1-\nu_2^2}{E_2} \tag{2}$$

$$\frac{1}{G^*} = \frac{1-\nu_1^2}{G_1} + \frac{1-\nu_2^2}{G_2} \tag{3}$$

$$G_{1,2} = \frac{E_{1,2}}{2\left(1+\nu_{1,2}\right)} \tag{4}$$

E_1 G_1 and ν_1 represent the Young's modulus of the indenter, its shear modulus and the Poisson's ratio, respectively. E_2, G_2 and ν_2 are the corresponding material parameters of the half-space.

Figure 5(d) shows the schematic diagram of the experimental system. Here, the friction coefficient of the slider in contact with the base is set to μ_1. The friction coefficient that cylindrical indenter drives the slider is set as μ. The indenter is made of a material with parameters of E_1, G_1 and ν_1, and elastic parameters of the slider material are E_2, G_2 and ν_2.

Further modeling is based on experimental data. Newton's second law then yields as follows:

$$M\ddot{X} = F_x - F_{base} - mg \tag{5}$$

F_x represents the frictional force between the indenter and slider. With the movement of the slider, a sliding friction force F_{base} goes up between the slider and the base. It is calculated as

$$F_{base} = \mathrm{sgn}\left(\dot{X}\right)\mu_1 F_y \tag{6}$$

Since in the numerical calculation, we can only use a discrete model as follows. In the circumstances, the value of the elongation of spring adds relative displacement $\Delta\tilde{x}$ that can be calculated as follows:

$$\Delta\tilde{x} = \left[x(t_i + \Delta t) - x(t_i)\right] - \left[X(t_i + \Delta t) - X(t_i)\right] \tag{7}$$

where t_i and Δt are the incrementally increasing time and the step of numerical time integration of Eq. (5) (time increment value).

The function $g(x)$ is found for a cylinder of finite length that is indented into a half-space. The form of this function is defined as follows:

$$g(x) = \beta\frac{L^2}{R}\left(\frac{\alpha L}{x} + 1\right)\exp\left(-\frac{\alpha L}{x}\right) \tag{8}$$

where L and R are the cylinder length and its radius, respectively. In addition, the ratio L/R determines the values of the parameters α and β.

The velocity is measured at a voltage with the saw-tooth wave of 100 $V_{p\text{-}p}$, and the duty ratio "S" is 90%, as shown in **Figure 5(e)**. As the frequency changes, the velocity trend shows a parabolic. And the different locking forces have different optimal driving frequencies. The x direction is taken as the moving direction of the slider. When the frequency is 850 Hz and locking force is 1 N, the maximum velocities in the positive direction and negative direction are 10.14 mm/s and 9.99 mm/s. When the frequency is 750 Hz and locking force is 2 N mm/s, the maximum velocities of the actuator are 8.56 and 8.72 mm/s in the positive direction and negative direction. When the frequency is 650 Hz and locking force is 3 N, the maximum velocities of the actuator are about 4.75 and 4.84 mm/s in the positive direction and negative direction.

As shown in **Figure 5(f)**, the solid lines and the dotted lines are the displacement curves and the simulation displacement curve of the slider under different locking forces. When the voltage is in a stage of rapid decrease, the dynamic friction

will be generated between the indenter and the slider. Meanwhile, the difference in the direction of the dynamic friction and the slider results in the production of the backward motion. Therefore, every step can produce a backward motion. Although it can be seen from the dotted line that the slider moves in forwarding and backward directions, the average velocity that is larger than zero will result in a net directional motion.

Experimental results indicate that the maximum loads tested in the experiment are 0.6 N, 0.9 N and 1.5 N under locking forces of 1 N, 2 N and 3 N, respectively. Furthermore, when the locking force and the minimum starting voltage are 2 N and 31.9 $V_{p\text{-}p}$ respectively, the forward and reversed displacement resolutions of the actuator are 91.1 nm and 74.4 nm. When the voltage and the frequency are 100 $V_{p\text{-}p}$ and 850 Hz, the maximum output velocity and the maximum load of the actuator in the positive x-direction is 10.14 mm/s and 1.5 N. When the load is 90 g, a locking force is 5 N, and the velocity is 5.48 mm/s, the actuator can reach the maximum efficiency of 0.57%.

3. Development of the hybrid excitation methods

3.1 Smooth driving method using ultrasonic friction reduction

3.1.1 Operation principle of smooth driving method

Figure 6(a) shows the working principle of the piezoelectric stick–slip actuator by traditional driving method (TDM), which includes the slow extension and rapid contraction stages of the traditional saw-tooth driving wave. As illustrated in **Figure 6(b)**, the smooth driving method (SDM) is realized by a composite wave, in which the composite wave includes a saw-tooth driving wave (SD-wave) and a sinusoidal friction regulation wave (SFR-wave), in which the SFR-wave can adjust the friction force between the frictional part and slider in resonant mode (RSFR-wave) or non-resonant mode (NSFR-wave) [15]. From the time A to B, the composite wave is equivalent to one part of the SD-wave. The piezoelectric element is excited to extend slowly, and the slider will move a distance together with the frictional part in the axial direction by a static friction force f_s. From the time B to C, the composite wave is composed by an SFR-wave and another part of the SD-wave, which means that the ultrasonic friction reduction is introduced into the composite wave to decrease the kinetic friction force f_d. Thus, the backward motion of the

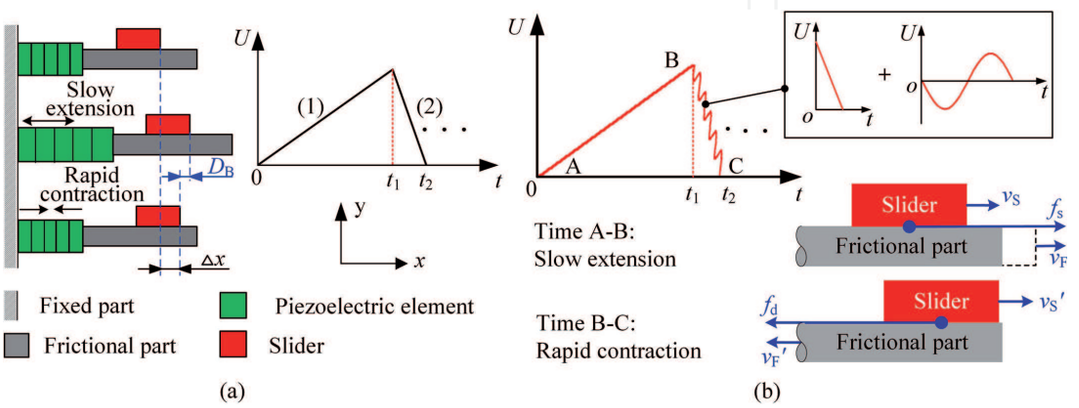

Figure 6.
Operation principle. (a) Principle of the traditional driving method. (b) Principle of the smooth driving method [15].

stick–slip actuator can be restrained. The continuous output movement is gained by repeating the above motion process. The reverse motion can be realized by reflecting the symmetry of the SDM.

3.1.2 Research on non-resonant mode smooth driving method

In this work, a non-resonant mode SDM is proposed to restrain the backward motion [15], which is realized by applying NSFR-wave to rapid deformation stage of the SD-wave. The specific work is as follows: the prototype includes a piezoelectric element, a frictional part, a slider and a preload mechanism, see **Figure 7(a)**. **Figure 7(b)** shows the experimental system of the prototype.

Figure 7(c) shows the amplitudes of the frictional part under the TDM and SDM. The frequency of the SD-wave is set as 800 Hz, and the voltage and frequency of the NSFR-wave are set as 4 $V_{p\text{-}p}$ and 40 kHz. It can be seen that the amplitude of the frictional part is not affected obviously under the excitation of the SDM. **Figure 7(d)** illustrates the displacement curves of the prototype with a load of 4 g. Compared with the TDM, the better performance is achieved by the SDM. To quantify the restraint degree of backward motion, the backward rate (denoted by ζ) is defined by a ratio of backward distance D_B and driving distance D_S. The results indicate that the backward rate is decreased markedly by 83%. The relationship between the velocity and NSFR-wave voltage is plotted in **Figure 7(e)**. The velocity with the NSFR-wave voltage of 0 $V_{p\text{-}p}$ represents the velocity under the excitation of the TDM; it is found that the velocity increases linearly with an increasing NSFR-wave voltage, and the velocity is obviously improved using the SDM relative to the TDM. **Figure 7(f)** shows the relationship between the velocity and voltage. The results indicate that there is a linear increasing tendency between the velocity and voltage.

3.1.3 Research on resonant mode smooth driving method

On the basis of our previous work, a resonant mode SDM is further developed to improve the performances of the actuators [16]. The resonant mode SDM is realized by applying a RSFR-wave to rapid deformation stage of the SD-wave. The relative

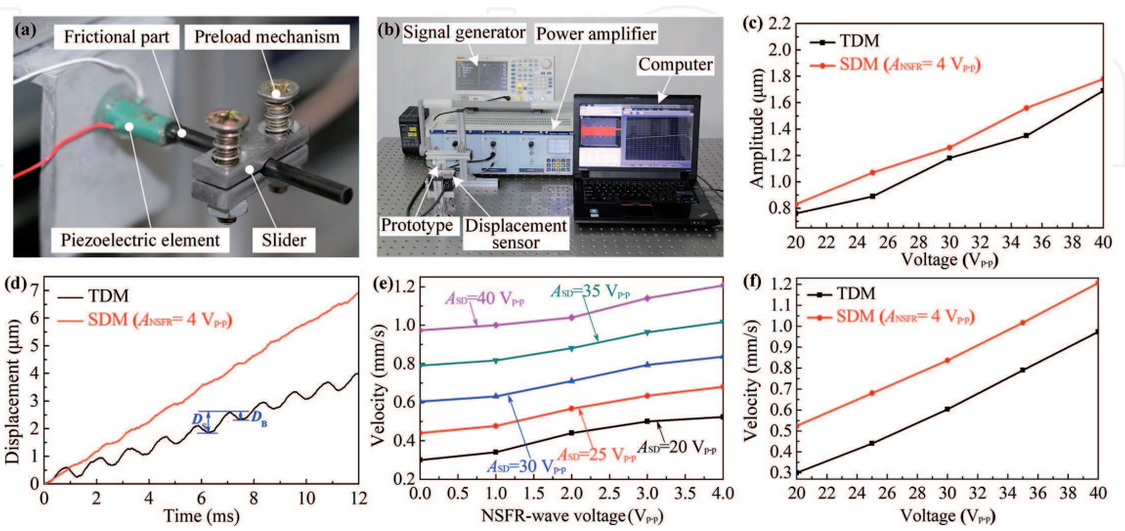

Figure 7.
Non-resonant mode SDM. (a) Prototype of the stick–slip actuator. (b) Experimental system. (c) Amplitude of the friction part excited. (d) Displacement curves of the prototype. (e) Velocity versus the NSFR-wave voltage. (f) Velocity versus the voltage [15].

research is as follows: the modal analysis of the stator is done by the FEM, aiming at obtaining the 1st longitudinal vibration mode, as illustrated in **Figure 8(a)**; and the theoretical result indicates that the resonant frequency of 38.55 kHz is obtained, which is considered the exciting frequency of the RSFR-wave.

Figure 8(b) shows the velocity versus the frequency of the RSFR-wave; the driving voltage of the SD-wave is set as 30 $V_{p\text{-}p}$, and the RSFR-wave voltage is selected as 6 $V_{p\text{-}p}$; the velocity of the actuator increases first and then decreases with an increasing frequency, and the maximum velocity is 0.41 mm/s under 39 kHz. Therefore, the RSFR-wave frequency of 39 kHz is chosen in subsequent experiments; there is a slight deviation between the test result and simulation result; the reasons may be caused by material errors between the model and the prototype, the omission of adhesive layers and the machining errors; besides, the comparative experiments of the SDM are also developed under the condition of 36 kHz and 42 kHz.

Figure 8(c) shows the relationship between the displacement and time; the displacement using the TDM shows a fluctuated curve and the backward motion is seen in every step; conversely, the backward motion is restrained by the SDM; the displacement increases linearly with an increasing time; the linearity is better when the frequency of RSFR-wave is 39 kHz, because the smaller kinetic friction is realized relative to the 36 kHz and 42 kHz. **Figure 8(d)** shows the relationship between the velocity and voltage; the velocity approximately follows a linear increased tendency with the voltage; the velocity using the TDM is 0.163 mm/s under 30 $V_{p\text{-}p}$; meanwhile, the velocities through the SDM are 0.332 mm/s, 0.403 mm/s and 0.370 mm/s (i.e. 36 kHz, 39 kHz, and 42 kHz), and the corresponding velocities can be effectively improved by 103.68%, 147.23% and 126.99% compared with the TDM.

Figure 8(e) expresses the variation of the velocity with an increasing load; the standard weight is used to investigate the load characteristics, which are added to the slider. The measure results indicate that the velocity decreases with an increasing load, and the load can reach 125 g utilizing the TDM; meanwhile, the maximum load excited by the SDM are 290 g, 360 g, and 315 g under 36 kHz, 39 kHz and 42 kHz; besides, under the same load, a higher velocity by the SDM is achieved at the RSFR-wave frequency of 39 kHz. **Figure 8(f)** shows that the relationship between the driving capacity and load; the driving capacity of the actuator increases first and then decreases with an increasing load, and the maximum

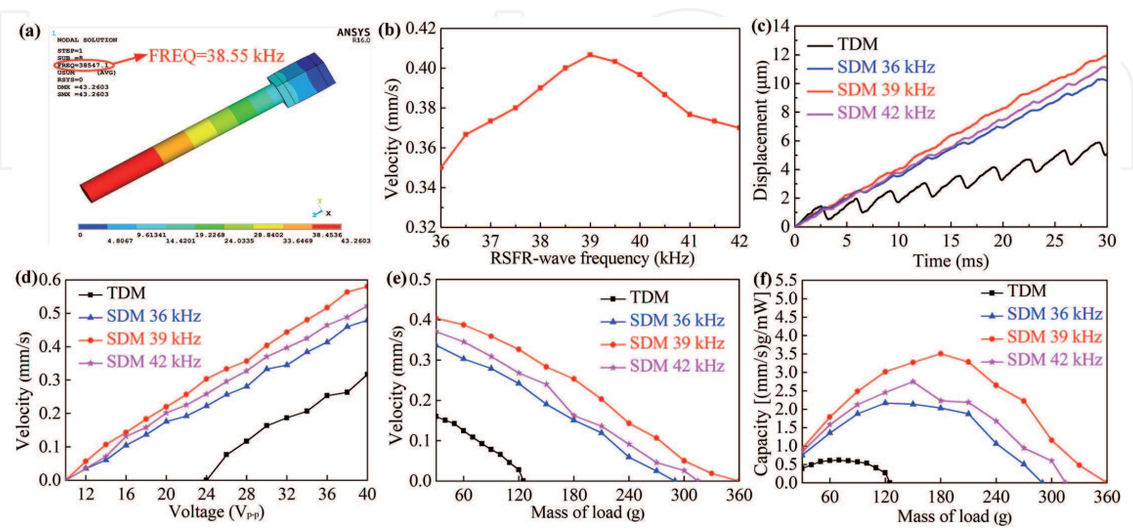

Figure 8.
Resonant mode SDM. (a) Modal analysis result of the stator. (b) Velocity versus the RSFR-wave frequency. (c) Displacement versus the time. (d) Velocity versus the voltage. (e) Velocity versus the mass of the load. (f) Driving capacity versus the mass of the load [16].

driving capacity using the TDM is 0.62 [(mm/s)g/mW] at 70 g. In contrast, the maximum driving capacities using the TDM (i.e. 36 kHz, 39 kHz and 42 kHz) are 2.18 [(mm/s)g/mW], 3.51 [(mm/s)g/mW] and 2.75 [(mm/s)g/mW] under 120 g, 180 g and 150 g; the driving capacities based on the SDM can be increased by 251.61%, 466.13% and 343.55% under the SFR-wave frequencies of 36 kHz, 39 kHz and 42 kHz.

3.1.4 Research on low voltage characteristics of smooth driving method

In this work, the low voltage characteristics of the SDM is researched [17]. **Figure 9(a)** and **(b)** show the relationships between the velocity and voltage in forward and reverse directions; the experiments are carried out under the same load of 4 g, and the frequencies of the SD-wave and the SFR-wave are 800 Hz and 40 kHz; the voltages of the SDM and TDM are increased from 2 $V_{p\text{-}p}$ to 10 $V_{p\text{-}p}$; the forward and reverse motions are changed by modifying the order of slow and rapid movements as 90% or 10%; the results indicate that the velocity of the actuator increase obviously as the voltage goes up. It also can be seen that the minimum input voltage is reduced from 3 $V_{p\text{-}p}$ to 2 $V_{p\text{-}p}$ under the SDM; there are the similar variation relations in the forward and reverse motions.

Figure 9(c) and **(d)** show the performances of the prototype with a load of 4 g by the SDM, in which the SDM is excited by the SD-wave voltage of 8 $V_{p\text{-}p}$ and SFR-wave of 1.6 $V_{p\text{-}p}$, and the voltage of the TDM is also 8 $V_{p\text{-}p}$. The results indicate that the prototype can achieve a stable operation at low voltage, and the backward motion is observed in every step; and the forward average effective displacement D_e is improved by 64%; the reverse average effective displacement D_e is improved by 55%; thus, the output displacement characteristics of the prototype is improved at a lower input voltage.

Figure 9(e) and **(f)** show the load characteristics of the actuator excited by the SDM and TDM, respectively; the output velocities of the actuator decrease as the load go up; compared with the TDM, the velocities can be improved obviously under the same load condition; the maximum load capacity of the actuator is 24 g when the voltages are 8 $V_{p\text{-}p}$ and 1.6 $V_{p\text{-}p}$, respectively, which is 2.4 times the load capacity of the actuator under the TDM. Therefore, the designed actuator excited by the SDM can achieve a larger load capacity.

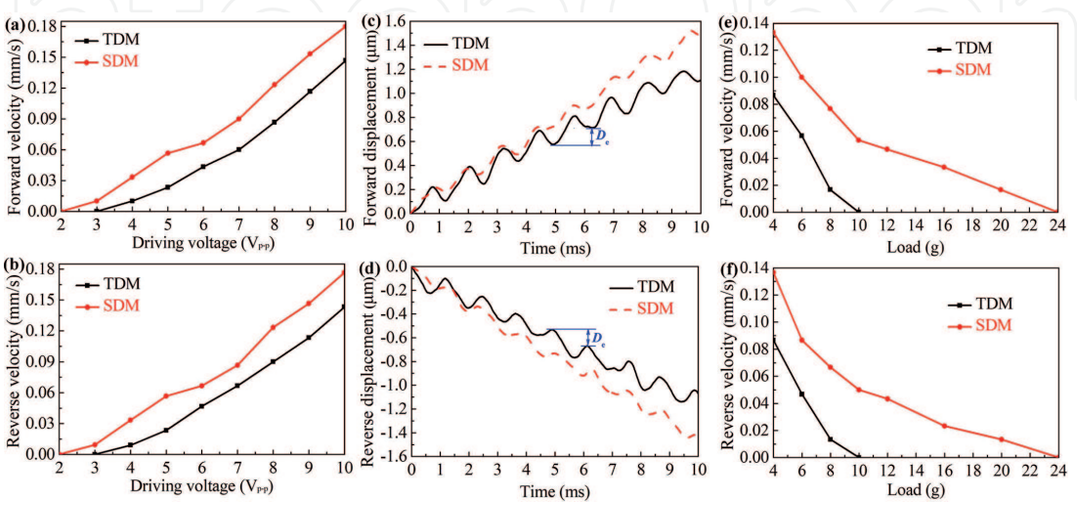

Figure 9.
Low voltage characteristics of the SDM. (a) Forward velocity versus the voltage. (b) Reverse velocity versus the voltage. (c) Forward displacement. (d) Reverse displacement. (e) Forward load characteristics. (f) Reverse load characteristics [17].

DOI: http://dx.doi.org/10.5772/intechopen.95536

3.1.5 Research on symmetry of smooth driving method

In this work, the symmetry of the SDM is also studied in detail [18]. **Figure 10(a)** and **(b)** show the relationship between the symmetry and velocity under the TDM and the SDM with an initial slider mass of 30 g; the voltage and frequency are 10 $V_{p\text{-}p}$ and 800 Hz. In terms of the TDM, the actuator under the symmetry of 50–80% and 20–50% cannot work properly, because the effective displacement cannot be generated; the maximum velocities are 0.21 mm/s and 0.20 mm/s under 95% and 5%; the symmetries between 80–95% and 5–20% are considered as the ideal working ranges. In terms of the SDM, the velocities under 95% and 5% can be improved obviously relative to the TDM, and the velocities can reach 0.24 mm/s and 0.23 mm/s. The maximum velocities in the forward and reverse directions can be achieved at 50%, and the corresponding velocities are 0.41 mm/s and 0.39 mm/s. It is found that the effective symmetry of the SDM is obviously widened relative to the TDM.

Figure 10(c) and **(d)** show the relationship between the load and velocity under the different symmetries, such as 90%, 70%, 50%, 30% and 10% in forward and reverse directions; the velocity of the actuator decreases with the increase of load; the velocities under 50%, 70% and 90% are almost equal at 110 g; when the load is less than 110 g, the maximum velocity can be achieved under 50%; when the load is greater than 110 g, the maximum velocity can be realized under 90%.

It is found that the asymmetrical SDM under 90% achieves the better load capacity when the SD-wave voltage is 10 $V_{p\text{-}p}$ for 800 Hz and the SFR-wave is 2 $V_{p\text{-}p}$ for 39 kHz; the actuator in the reverse direction can also achieve the similar load characteristics; the larger stiffness is obtained under 90% and 10%.

The relationship between the load and driving capacity is illustrated in **Figure 10(e)** and **(f)**; the driving capacities of the actuator can reach 7.92 [(mm/s) g/mW] and 6.77 [(mm/s)g/mW] under 70% and 90%; meanwhile, the driving capacities of the actuator can reach 8.42 [(mm/s)g/mW] and 7.11 [(mm/s)g/mW] under 30% and 10%. The results indicate that the symmetrical SDM such as 50% can achieve larger driving capacity relative to the asymmetrical SDM, such as 90%, 70%, 30% and 10%.

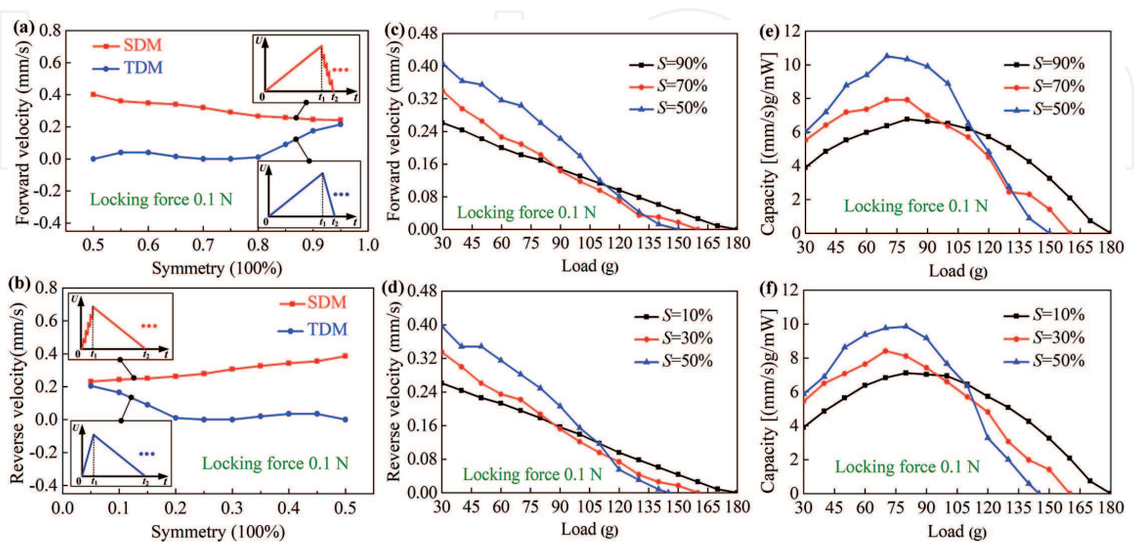

Figure 10.
Symmetry of the SDM. (a) Forward velocity versus the symmetry. (b) Reverse velocity versus the symmetry. (c) Forward velocity versus to the load under 50%, 70% and 90%. (d) Reverse velocity versus to the load under 10%, 30% and 50%. (e) Forward driving capacity versus the load under 50%, 70% and 90%. (f) Reverse driving capacity versus the load under 10%, 30% and 50% [18].

3.2 Direction-guidance hybrid method for high speed

3.2.1 Operation principle of direction-guidance hybrid method

To improve the speed of the stick–slip actuators, a direction-guidance hybrid method (DGHM) is proposed in this work [19]. The DGHM is a synthetic composite waveform, as shown in **Figure 11(a)**, which is mainly composed of a direction-guidance (DG) waveform and a resonance drive (RD) waveform. The stator excited by the DG waveform to produce a pre-deformation with a lateral motion, which is of great significance to the output characteristics of the actuator. The direction of the slider can be guided by the lateral motion of the stator; besides, the locking force can be adjusted to achieve better output performance. After that, the high speed performance of the actuator can be achieved at a resonant frequency of the RD waveform.

The operation principle of the actuator under the DGHM is shown in **Figure 11(b)**. The specific operations are as follows:

Stage I: at time t_0, the piezoelectric stack without input voltage, the length of the stack is l_0, and the slider and the stator are at the initial position. Due to the existence of the initial locking force, there is a pair of equal and opposite interaction forces (F_{I0} and F_{R0}) between the driving foot and the slider.

Stage II: the length of the stack extends to l_1 quickly excited by the DG waveform at time t_1 so that stator is produced an oblique deformation. The position of the driving foot is moved from position ① to position ②, which causes a pre-deformation of the stator. At the same time, the slider will produce a displacement of Δd_1 along the ox axis with the help of the driving foot. In addition, the interaction force becomes F_{I1} and F_{R1} after incrementing ΔF ($|F_{I1}| = |F_{R1}| = |F_{I0}| + |\Delta F|$), which can further increase the load capacity and horizontal thrust of the actuator within a proper range of regulation.

Stage III: the stack is excited by the DGHM at time t_2. The excitation voltage of the DG waveform is kept constant. The RD waveform is composed of high frequency sine waveforms with the period of T_R. The stack undergoes an elongation and contraction between the lengths of l_1 and l_2 in each cycle. Correspondingly, the driving foot vibrates rapidly between the positions of ② and ③. During the time of T_R, a displacement Δd_2 of the slider is produced along the ox axis. The velocity of

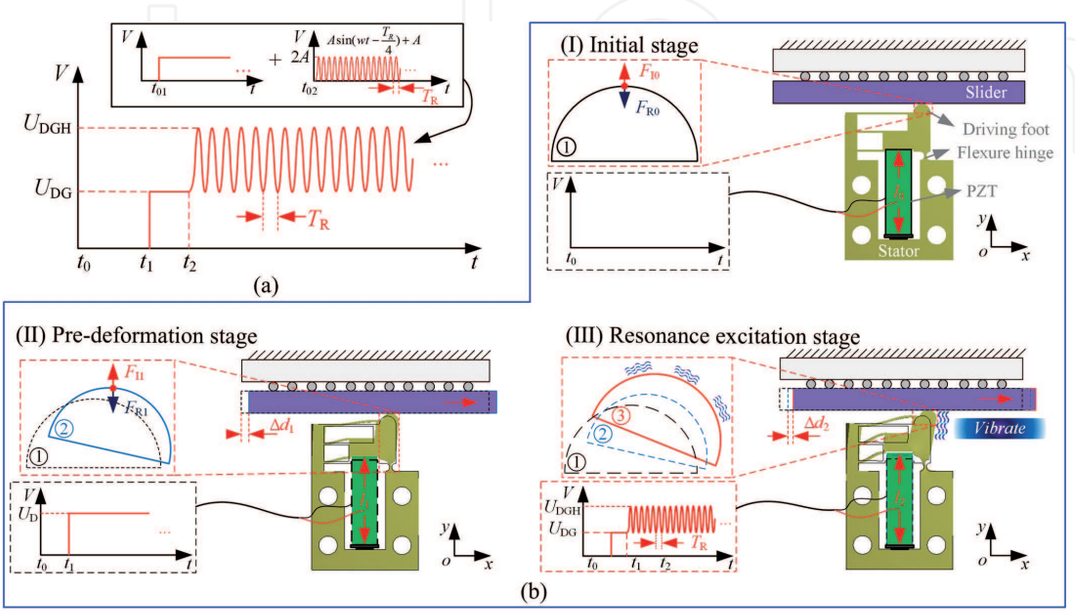

Figure 11.
Operation principle of the DGHM. (a) Schematic of the DGHM. (b) Specific operations of the DGHM [19].

the actuator is v ($v = f_R \times \Delta d_2$), where f_R is the frequency of the RD waveform. Even at a low voltage, the actuator can achieve a high speed by the DGHM.

3.2.2 Research on direction-guidance hybrid method

The related work based on the DGHM is as follows [19]. As shown in **Figure 12(a)**, an actuator is fabricated to verify the feasibility of the DGHM. In the first place, the influence of the DG waveform with different amplitudes of the driving foot is analyzed by the FEM. The point P is chosen as the reference point, which represents the contact point between the slider and the driving foot, as shown in **Figure 12(c)**. **Figure 12(b)** simulates the equivalent stress of the stator and deformation of the point P when the piezoelectric stack inputs different displacements driven by the DG waveform. The displacement of the point P increases linearly in the ox and oy axes directions with the increase of the input displacement, which verifies the effectiveness of the DG waveform. Besides, the equivalent stress of the stator is 202.46 MPa with the input of 10 μm. Afterwards, the modes of the stator are analyzed to make the actuator operate at a resonant frequency. As shown in **Figure 12(c)**, when the frequency of RD waveform is at fourth mode (around 30.57 kHz), the proposed actuator has the potential to achieve higher speed.

The actuator is manufactured and the test system is built, as shown in **Figure 12(d)**. Firstly, the effect of the voltage of DG waveform on the displacement of the driving foot is explored. As shown in **Figure 12(e)**, the driving foot can achieve displacement along

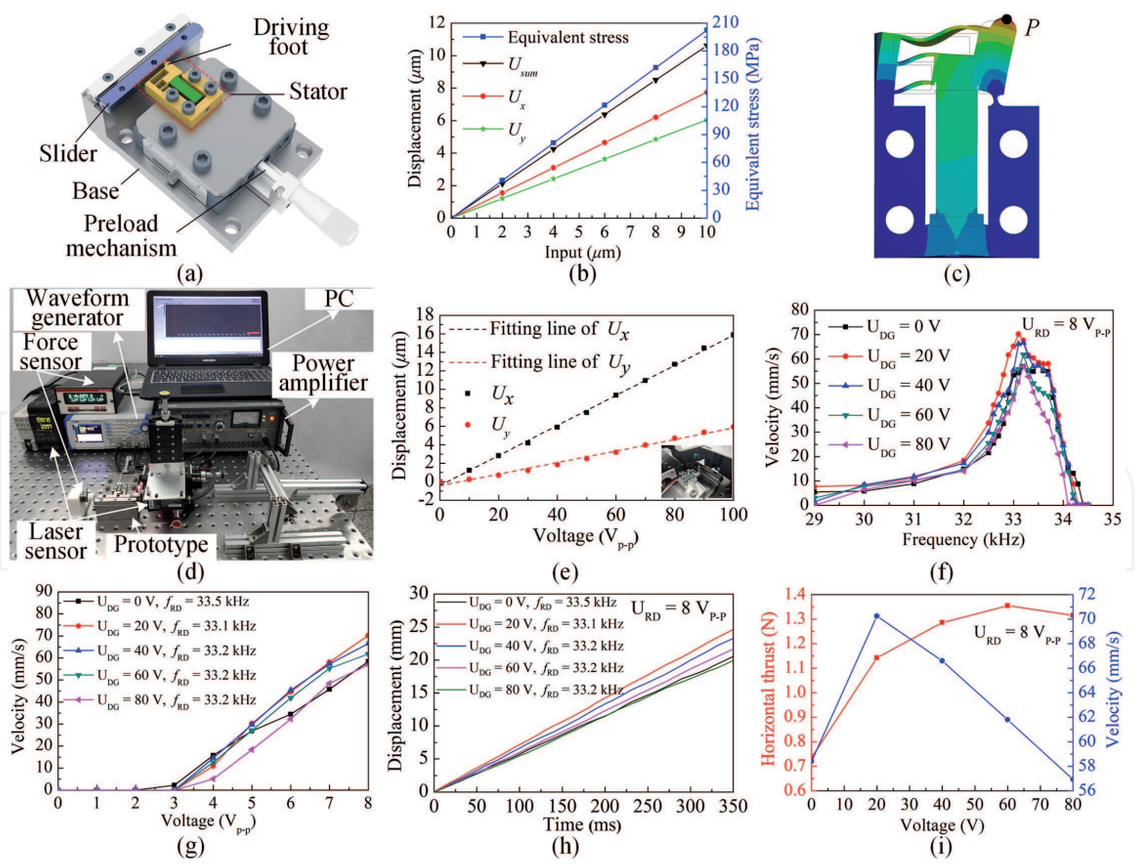

Figure 12.
Research on DGHM. (a) Configuration of the proposed design. (b) Simulation of the stator by FEM. (c) Fourth mode of the stator. (d) The experimental system and the prototype. (e) The relationship between the displacement of the reflector and the voltage of DG waveform. (f) The relationship between driving frequency of DGHM and output velocity. (g) The relationship between the velocity and the voltage of RD waveform under the different voltages of DG waveform. (h) The displacement of the prototype at different voltages of DG waveform. (i) The horizontal thrust and the velocity versus at the voltages of DG waveform under the DGHM [19].

the positive direction of the *ox* and *oy* axes. With the increase of the voltage of the DG waveform, the displacements in both directions have a good linear relationship, which shows that the actuator can produce a pre-deformation by the aid of the proposed excitation method.

Under the condition of an initial preload force of 0.5 N, a series of experiments are carried out to explore the output characteristics of the proposed actuator. As shown in **Figure 12(f)**, the output speed and the frequency of the RD waveform are studied under different voltage of the DG waveform to determine the optimal driving frequency of the RD waveform. At different voltages of the DG waveform, the optimal frequencies of the RD waveform are around 33 kHz, which is close to the frequency simulated by FEM. When the DG waveform is 20 V and the RD waveform is 8 V_{P-P} and 33.1 kHz, the actuator reaches the maximum velocity of 70.26 mm/s.

Under different DG waveform voltages, the velocities of the actuator versus voltages of the RD waveform are measured. It can be seen from **Figure 12(g)** that the velocity increases as the RD waveform voltage. The actuator starts to move as the voltage of RD waveform is about 3 V_{p-p}. At the voltage of 8 V_{p-p}, the velocity reaches the maximum and it can be further improved by increasing the voltage of the RD waveform. As shown in **Figure 12(h)**, the displacement curve at different voltages of DG waveform shows that the DGHM can make the actuator move stably. As shown in **Figure 12(i)**, the horizontal thrust and velocity at a different voltage of the DG waveform are explored which shows that the actuator can achieve the large horizontal thrust or the relatively high velocity under the DGHM. Although the initial locking force is 0.5 N, the actuator can achieve the maximum horizontal thrust of 1.36 N when the voltage of DG waveform is 60 V.

4. Conclusions

A comprehensive work of piezoelectric stick–slip actuators was presented to improve their output characteristics. This work divided our team's stick–slip actuators into two categories based on the research ideas, including structural designs and driving methods.

In terms of structural designs, the trapezoid-type actuator increased static friction force in slow extension stage and decreased kinetic friction force in rapid contraction stage by lateral motion, which improved the forward performance. The actuators with asymmetrical flexure hinges widened the structure forms of the actuator and improved the velocity, load and efficiency. The mode conversion actuator could be used in precision positioning platform and ultra-precision machining due to its nanometer resolution. Besides, an actuator with a coupled asymmetrical flexure hinge mechanism realized the bidirectional motion.

In terms of driving methods, a non-resonant mode smooth driving method (SDM) based on ultrasonic friction reduction was proposed, and the backward motion was restrained during the rapid contraction stage. Compared with non-resonant mode SDM, the resonant mode SDM achieved a higher velocity, larger load and smoother displacement. Besides, the proposed SDM achieved better low voltage characteristics and widened the symmetry relative to the traditional driving method. Finally, a direction-guidance hybrid method (DGHM) could achieve superior performance, especially for high speed.

Acknowledgements

This work was financially supported by the Jilin Province Science and Technology Development Plan Item (No. 20150312006ZG), the Postdoctoral

Science Foundation of China (No. 2015 M571356), the Key Projects of Science and Technology Development Plan of Jilin Province (No. 20160204054GX), the Project of Industrial Technology Research and Development of Jilin Province Development and Reform Commission (No. 2019C037-6) and the Science and Technology Development Plan of Jilin Province (Nos. 20190201108JC and 20200201057JC).

Conflict of interest

The author(s) declared no potential conflicts of interest with respect to the research, authorship, and/or publication of this article.

Author details

Tinghai Cheng[1,2*], Xiaosong Zhang[1], Xiaohui Lu[1], Hengyu Li[3], Qi Gao[2] and Guangda Qiao[1]

1 School of Mechatronic Engineering, Changchun University of Technology, Changchun, China

2 Beijing Institute of Nanoenergy and Nanosystems, Chinese Academy of Sciences, Beijing, China

3 State Key Laboratory of Robotics and System, Harbin Institute of Technology, Harbin, China

*Address all correspondence to: chengtinghai@binn.cas.cn

References

[1] Hunstig M. Piezoelectric inertia motors—a critical review of history, concepts, design, applications, and perspectives. Actuators. 2017;6:35. DOI: 10.3390/act6010007

[2] Qin F, Tian L, Huang H, Wang J, Liang T, Zu X, Zhao H. Actively controlling the contact force of a stick-slip piezoelectric linear actuator by a composite flexure hinge. Sensors and Actuators a-Physical. 2019;299:10. DOI: 10.1016/j.sna.2019.111606

[3] Guo Z, Tian Y, Zhang D, Wang T, Wu M. A novel stick-slip based linear actuator using bi-directional motion of micropositioner. Mechanical Systems and Signal Processing. 2019;128:37-49. DOI: 10.1016/j.ymssp.2019.03.025

[4] Lee J, Kwon W, Kim K, Kim S. A novel smooth impact drive mechanism actuation method with dual-slider for a compact zoom lens system. Review of Scientific Instruments. 2011;82:8. DOI: 10.1063/1.3624701

[5] Peng J, Chen X. Modeling of piezoelectric-drive stick-slip actuator. IEEE/ASME Transactions on Mechatronics. 2011;16:394-399. DOI: 10.1109/tmech.2010.2043849

[6] Hunstig M, Hemsel T, Sextro W. Modelling the friction contact in an inertia motor. Journal of Intelligent Material Systems and Structures. 2013;24:1380-1391. DOI: 10.1177/1045389X12474354

[7] Li J, Zhou X, Zhao H, Shao M, Hou P and Xu X. Design and experimental performances of a piezoelectric linear actuator by means of lateral motion. Smart Materials and Structures. 2015;24:065007. DOI: 10.1088/0964-1726/24/6/065007

[8] Wang S, Rong W, Wang L, Pei Z, Sun L. Design, analysis and experimental performance of a bionic piezoelectric rotary actuator. Journal of Bionic Engineering. 2017;2:348-355. DOI: 10.1016/s1672-6529(16)60403-1

[9] Wen J, Ma J, Zeng P, Cheng G & Zhang Z. A new inertial piezoelectric rotary actuator based on changing the normal pressure. Microsystem Technologies. 2013;19:277-283. DOI: 10.1007/s00542-012-1684-9

[10] Cheng T, He M, Li H, Lu X, Zhao H, Gao H. A novel trapezoid-type stick–slip piezoelectric linear actuator using right circular flexure hinge mechanism. IEEE Transactions on Industrial Electronics. 2017;64:5545-5552. DOI: 10.1109/TIE.2017.2677318

[11] Gao Q, He M, Lu X, Zhang C, Cheng T. Simple and high-performance stick-slip piezoelectric actuator based on an asymmetrical flexure hinge driving mechanism. Journal of Intelligent Material Systems and Structures. 2019;30:2125-2134. DOI: 10.1177/1045389X19862376

[12] Gao Q, Li Y, Lu X, Zhang C, Zhang X, Cheng T. A piezoelectric stick-slip linear actuator with a rhombus-type flexure hinge mechanism by means of parasitic motion. Review of Scientific Instruments. 2019;90:096102. DOI: 10.1063/1.5082856

[13] Zhang X, Yu Y, Gao Q, Qiao G, Li Z, Lu X, Cheng T. A stick-slip linear piezoelectric actuator with mode conversion flexure hinge driven by symmetrical waveform. Smart Materials and Structures. 2020;29:055035. DOI: 10.1088/1361-665X/ab7f42

[14] Lu X, Gao Q, Gao Q, Yu Y, Zhang X, Qiao G, Zhao H, Cheng T. Design, modeling, and performance of a bidirectional stick-slip piezoelectric actuator with coupled asymmetrical flexure hinge mechanisms. Journal

of Intelligent Material Systems and Structures, 2020;31:1961-1972. DOI: 10.1177/1045389X20942325

[15] Wang L, Chen D, Cheng T, He P, Lu X, Zhao H. A friction regulation hybrid driving method for backward motion restraint of the smooth impact drive mechanism. Smart Materials and Structures. 2016;25:085033. DOI: 10.1088/0964-1726/25/8/085033

[16] Cheng T, Li H, He M, Zhao X, Lu X, Gao H. Investigation on driving characteristics of a piezoelectric stick-slip actuator based on resonant/off-resonant hybrid excitation. Smart Materials and Structures. 2017;26:035042. DOI: 10.1088/1361-665X/aa5c2c

[17] Cheng T, Lu X, Zhao H, Chen D, He P, Wang L, Zhao X. Performance improvement of smooth impact drive mechanism at low voltage utilizing ultrasonic friction reduction. Review of Scientific Instruments. 2016;87:085007. DOI: 10.1063/1.4960392

[18] Li H, Li Y, Cheng T, Lu X, Zhao H, Gao H. A Symmetrical Hybrid Driving Waveform for a Linear Piezoelectric Stick-Slip Actuator. IEEE Access. 2017;5:16885-16894. DOI: 10.1109/access.2017.2744498

[19] Yu Y, Gao Q, Qiao G, Zhang X, Lu X, Cheng T. A direction-guidance hybrid excitation method for inertial flexure hinge piezoelectric actuator with high speed performance. Sensors and Actuators A: Physical. 2020;314:112229. DOI: 10.1016/j.sna.2020.11222